Flow generated noise produced by a blunt edged plate in a water tunnel

P. Croaker and J. Venning and M. Karimi and P. A. Brandner and C. Doolan and N. Kessissoglou

Abstract A numerical and experimental investigation into the flow and noise produced by a blunt-edged flat plate with a Reynolds number based on chord of 6.8 million and a Mach number of 0.0053 is presented. The flat plate had a 4:1 aspect ratio elliptic leading edge and a square trailing edge with a thickness-to-chord ratio of 0.0054. Experimental measurements were performed in a reverberant water tunnel. Pressure sensors were flush mounted on the top, bottom and rear faces of the blunt edge at the mid-span plane. Further, a hydrophone was mounted in a flooded cavity in the tunnel wall beneath a polyurethane diaphragm. An analytical model for trailing edge scattering was extended to account for near-field effects and to consider reflection of pressure waves by the tunnel walls. A large eddy simulation was also conducted, with hydrodynamic pressures on the surface of the plate extracted and combined with the analytical scattering model to predict the pressure fluctuations

---

P. Croaker

Maritime Division, Defence Science and Technology Group, Melbourne, Australia, e-mail: `paul.croaker@dst.defence.gov.au`

J. Venning

Cavitation Research Laboratory, University of Tasmania, Launceston, Australia, e-mail: `james.venning@utas.edu.au`

M. Karimi

Centre for Audio, Acoustics and Vibration, University of Technology Sydney, Sydney, Australia, e-mail: `Mahmoud.Karimi@uts.edu.au`

P. A. Brandner

Cavitation Research Laboratory, University of Tasmania, Launceston, Australia, e-mail: `p.brandner@utas.edu.au`

C. Doolan

School of Mechanical and Manufacturing Engineering, University of New South Wales, Sydney, Australia, e-mail: `c.doolan@unsw.edu.au`

N. Kessissoglou

School of Mechanical and Manufacturing Engineering, University of New South Wales, Sydney, Australia, e-mail: `n.kessissoglou@unsw.edu.au`

on the wall of the water tunnel. Numerical predictions are found to agree well with the experimental measurements.

1 Introduction

The aim of the present work is to numerically predict flow generated noise for hydroacoustic applications, with a particular focus on the generation and propagation of flow generated pressure waves for confined flows, such as axial and centrifugal pumps. One of the mechanisms by which these devices produce sound is the scattering of boundary layer pressures from trailing edges. This work focuses on the development of a numerical technique to estimate the near-field radiation of flow generated pressures from trailing edges in water, with experimental measurements also obtained to validate the numerical technique.

Development and application of flow generated noise prediction techniques have focused almost exclusively on aerodynamically produced sound, see for example [1, 2, 3, 4]. The vast majority of analytical methods derived to estimate flow generated noise focus on the far-field acoustic response in air [5, 6, 7, 8]. Further, a large number of high quality aeroacoustic flow and noise measurements have been conducted [9, 10, 11, 12]. These studies provide a valuable source of benchmark data for development of predictive numerical models. Applying aeroacoustic prediction techniques to study the generation and propagation of flow generated noise in water is not always straightforward. The characteristic Reynolds number for marine applications is typically very high. This is accompanied by a very low Mach number which further widens the separation of hydrodynamic and acoustic scales that are present in aeroacoustic problems. Recent work of Ianniello [13, 14, 15, 16] and Cianferra et al. [17] has suggested that non-linear flow noise sources, traditionally neglected in low Mach number aeroacoustics, may make a significant contribution to the flow generated noise produced by objects moving in water. Ianniello et al. [13, 14, 15] combined the Ffowcs-Williams and Hawkings (FW-H) analogy with hydrodynamic data from incompressible computational fluid dynamics (CFD) analyses to demonstrate that the non-linear flow noise sources make a significant contribution to the far-field noise produced by marine propellers. Cianferra et al. [17] extended this work to consider non-rotating bodies moving in water and concluded that non-linear flow noise sources may also make a significant contribution to the far-field sound produced by non-rotating bodies. However, hydroacoustic scattering from sharp geometrical features is not captured when the Ffowcs-Williams and Hawking analogy is combined with hydrodynamic data from incompressible CFD simulations. This is because the incompressible CFD simulation does not capture the propagation and interaction of flow generated pressures with the trailing edge geometry [18]. As such, the technique developed by Ianniello et al. cannot be applied to predict the noise produced by trailing edge scattering and an alternate strategy is pursued here.

In the present work, experiments on the flow and noise produced by a blunt edged flat plate are conducted in a cavitation tunnel. A computational fluid dynamics (CFD) analysis of the flow is also conducted using large eddy simulation (LES). The surface pressure on the plate is extracted and combined with an analytical trailing

edge scattering model originally proposed by Amiet [6] and modified by Roger and Moreau to account for leading edge back-scatter [8, 19]. The analytical model is modified here to account for the near-field effects and reflection of pressure waves off the tunnel walls. Numerical results and measured data are compared and discussed.

2 Experimental Setup

All experiments were carried out in the closed recirculating variable-pressure water tunnel of the Cavitation Research Laboratory at the Australian Maritime College (AMC). A schematic diagram of the tunnel circuit is shown in Fig. 1. The tunnel test section is 0.6 m square by 2.6 m long and the tunnel volume is 365 m^3 with demineralised water as the working fluid. The nominal operating velocity and absolute-pressure ranges are 2 to 13 m/s and 4 to 400 kPa, respectively. The circuit has low background noise and vibration levels due to low velocities and isolation from the surrounding building and all noise-generating machinery. The cavitation tunnel design and specification is described in detail in [20].
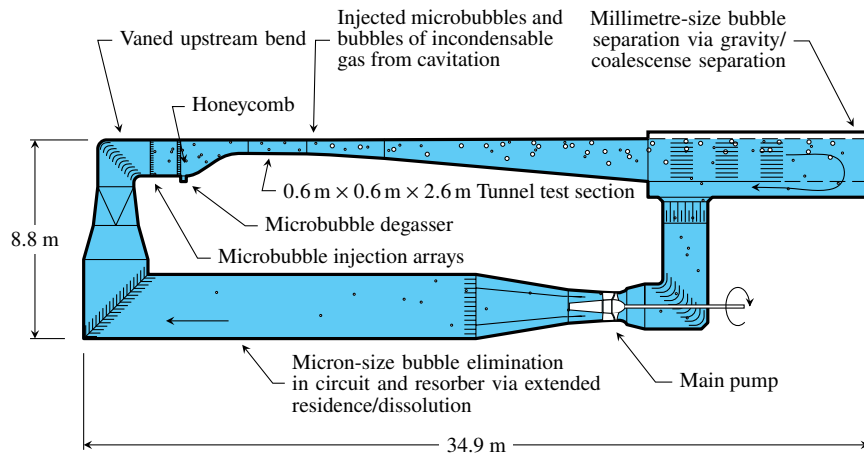

Fig. 1: Schematic diagram of the AMC variable-pressure water tunnel. Circuit architecture for continuous removal of microbubbles or large volumes of injected incondensable gas as well as ancillaries for microbubble seeding and for degassing of water are shown. Microbubbles may be either injected for modelling cavitation nucleation or generated by the cavitation itself.

A stainless steel rectangular plate with elliptical leading edge of 4:1 aspect ratio was mounted vertically at the mid-span of the tunnel test section as shown in Fig. 2. The thickness H is 46 mm and chord L is 850 mm, giving a test section blockage of 7.7%. The freestream velocity was maintained at 7.93 m/s such that the chord-based

Reynolds number was 6.8×10^6 and the Mach number was 5.3×10^{-3}. The freestream absolute pressure was maintained at 105 kPa and no cavitation was observed.
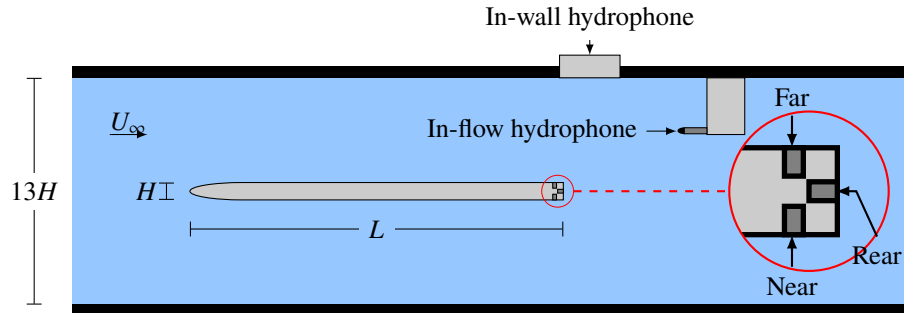

Fig. 2: Top view of the bluff plate in the AMC tunnel test section.

The hydrodynamic noise was measured with two hydrophones and three pressure sensors. The hydrophones were Brüel & Kjær type 8103 models with a frequency range up to 180 kHz. One hydrophone was mounted in the tunnel wall 70 mm downstream of the trailing edge of the plate. The wall-mounted hydrophone was installed in a flooded cavity behind a 149 mm diameter, 10 mm thick polyurethane diaphragm as described in [21]. The acoustic impedance of polyurethane is similar to water, thus providing a near reflection-free acoustic interface. The large sensing area of the diaphragm provides attenuation of the turbulent boundary layer noise. The in-flow hydrophone was positioned 150 mm away from the tunnel wall and 280 mm downstream of the plate trailing edge. Both these hydrophone signals were conditioned with a Brüel & Kjær type 2692 charge amplifier with a 0.1 Hz low-pass filter and a 100 kHz high-pass filter. Signals were recorded for 81 s with an acquisition rate of 204.8 kHz. Only results for the wall-mounted hydrophone are presented here as the measured flow generated noise relative to background noise is greatest for this hydrophone.

The three pressure sensors were quartz-type PCB 105C02 sensors with 2.5 mm diameter sensing surfaces and a resonant frequency of over 250 kHz. Two pressure sensors were mounted in the two sides of the plate, 23 mm upstream of the trailing edge. These are labelled 'near' and 'far' and are situated 311.5 mm and 288.5 mm from the tunnel ceiling, respectively. The third pressure sensor is located in the rear surface of the plate and 300 mm from the ceiling. These signals were conditioned with a Kistler 5080A amplifier.

3 Numerical Flow-Induced Noise Prediction

3.1 Hydrodynamic Data and Acoustic Sources

An LES of the unsteady flow field around the plate was performed by filtering the incompressible Navier-Stokes equations to separate the hydrodynamic fluctuations into resolved and sub-grid scale components. The filtered incompressible Navier-Stokes equations are given by

$$\rho_0 \frac{\partial \hat{u}_i}{\partial t} + \rho_0 \frac{\partial}{\partial y_i} \left(\hat{u}_i \hat{u}_j \right) = -\frac{\partial \hat{p}}{\partial y_j} + 2 \left(\mu_0 + \mu_{\text{SGS}} \right) \frac{\partial}{\partial y_j} \hat{S}_{ij} \tag{1}$$

$$\frac{\partial \hat{u}_j}{\partial y_j} = 0 \tag{2}$$

where $\hat{p}$ is the filtered pressure and $\hat{u}_i$ represents components of the resolved velocity vector. μ_0 and ρ_0 are the viscosity and density of the fluid at rest. $\hat{S}_{ij}$ is the strain rate tensor of the resolved scales. The wall-adapting local eddy-viscosity model in [22] was used to define the eddy viscosity, μ_{SGS}, which accounts for the influence of the sub-grid scales on the filtered motion. Due to the high Reynolds number, it is computationally impractical to resolve the velocities into the plate viscous sublayer. Instead, the wall model of Spalding [23] is used to model the effect of the near wall stresses on the flow. Equation (2) was solved using OpenFOAM [24].

A hybrid mesh comprising a fully structured core mesh around the plate and in the wake region was constructed. An unstructured mesh was also created away from the plate to reduce cell count. Further, only a 0.07 m spanwise section of the model has been considered with periodic boundary conditions applied to further reduce the total number of CFD mesh cells. A baseline mesh was created with near wall cell sizes of $x^+ \approx 100$, $y^+ \approx 24$ and $z^+ \approx 120$, resulting in a total of 22×10^6 hexahedral cells. A systematic grid refinement procedure was then followed to investigate the influence of mesh resolution on the accuracy of the LES results. For each subsequent mesh, the grid size in one of the principal directions was halved, with the mesh first refined in the spanwise, then streamwise and finally wall normal directions. Table 1 presents a summary of the different LES meshes. Similar to the experimental set-up, the plate is mounted in a water tunnel with cross-section of $0.6\,\text{m} \times 0.6\,\text{m}$. The CFD model extends 1.5 m upstream of the leading edge and 3.65 m downstream of the trailing edge. Fig. 3 shows the CFD model and associated mesh.

The pressure implicit with splitting of operator algorithm was used to deal with the pressure-velocity coupling during solution of the LES equations. A second-order backward implicit scheme was used for the temporal discretisation. A blended spatial differencing scheme was used with 80% second order central differencing and 20% second order upwind differencing for the non-linear terms in the momentum equations. A standard second order central differencing scheme was used for all other spatial discretisations.

Table 1: CFD mesh resolutions used for current study

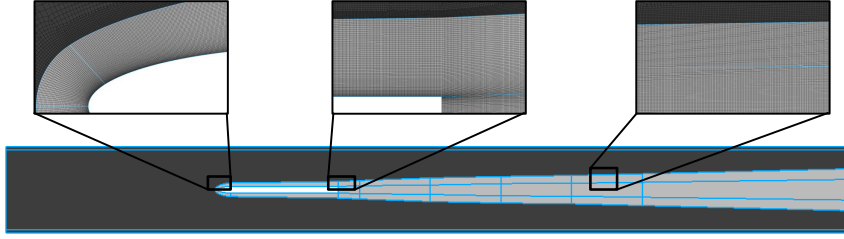| Mesh	x^+	y^+	z^+	Cells
1	100	24	120	22×10^6
2	100	24	60	44×10^6
3	50	24	60	88×10^6
4	50	12	60	120×10^6

Fig. 3: CFD mesh model for the blunt edge flat plate. Inserts show the CFD mesh near the leading and trailing edges and the far wake.

The transient simulation was executed with a time step size of 2.5×10^{-6} s and was allowed to progress until the flow field achieved quasi-periodicity. Recording of the surface pressures on the plate then commenced with the pressure stored at intervals of 5×10^{-4} s. Time histories of the surface pressures were divided into equal segments with a length of 458 time steps with 50% overlap. A Hanning window function was applied to each segment of the surface pressure time histories before converting them to frequency spectra.

4 Propagation of Flow-Induced Pressure Waves

4.1 Analytical Scattering and Propagation

A simple modification to the analytical scattering technique originally developed by Amiet [6] and later extended by Roger and Moreau [8] is proposed to investigate scattering and propagation of the flow-induced pressure waves that are generated in the tunnel. Fig. 4 shows the idealised geometry and coordinate system used for prediction of the flow-induced pressure wave propagation.

For a surface pressure distribution of wavenumber $\mathbf{K} = (K_1, K_2)$, with K_1 and K_2 respectively denoting the streamwise and spanwise wavenumbers, Roger and
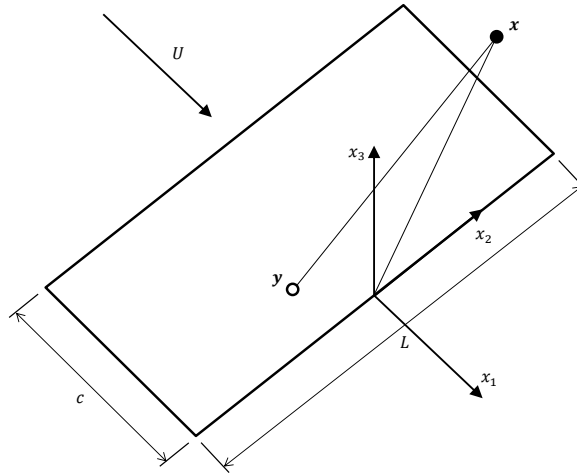
Fig. 4: Schematic diagram showing geometry and coordinate system used for trailing edge scattering.

Moreau [8, 19] derived the following expression for the far-field pressure produced by trailing edge scattering and radiation from the trailing edge of a flat plate

$$p_K(\mathbf{x}, \omega) = \frac{-\mathrm{i}\, k_a x_3}{4\pi S_0^2} \int_{-2b}^{0} \int_{-L/2}^{L/2} \Delta P(K_1, K_2)\, \mathrm{e}^{\mathrm{i}\, k_a R_t}\, \mathrm{d}\, y_1\, \mathrm{d}\, y_2 \tag{3}$$

p_K is the far-field pressure produced by a surface pressure distribution denoted by $\Delta P(K_1, K_2)$ associated with wavenumbers K_1 and K_2. ω is the angular frequency and $k_a = \omega/c_0$ is the acoustic wavenumber with c_0 representing the speed of sound in the fluid at rest. R_t represents the distance between source point $\mathbf{y}$ and field point $\mathbf{x}$. In the original work of Roger and Moreau [8], the effect of background convection on acoustic waves was included. However, for applications in water with very low Mach number, the effect of background convection on the propagation of pressure waves becomes negligible. The distance between source and field points can be expressed by

$$R_t = S_0\left(1 - \frac{x_1 y_1 + x_2 y_2}{S_0^2}\right) \tag{4}$$

where $S_0^2 = x_1^2 + x_2^2 + x_3^2$ is the distance from the coordinate system origin at the trailing edge to the far-field location $\mathbf{x}$. This representation of distance is convenient for use with analytical scattering methods as the contributions from individual components

of the source vector **y** are decoupled. However, it must be noted that equation (4) is a simplification of the distance and only approaches the true distance between source and field points when $|\mathbf{x}| >> |\mathbf{y}|$.

Amiet [6] and Roger and Moreau [8] have shown that the autospectral density of the acoustic pressure at a far-field receiver location is given by

$$S_{PP,\text{ff}}(\mathbf{x}, \omega) = \left(\frac{\omega x_3 Lb}{2\pi c_0 S_0^2}\right)^2 \frac{1}{b} \int_{-\infty}^{\infty} \Pi_0\left(\frac{\omega}{U_c}, K_2\right) \text{sinc}^2\left(\frac{L}{2b}\left(\bar{K}_2 - \bar{k}_a \frac{x_2}{S_0}\right)\right)$$
$$\times \left| I\left(\bar{K}_c, \bar{K}_2\right)\right|^2 d\bar{K}_2 \tag{5}$$

where x_i represents the ith component of the far-field receiver position vector. L is the span of the plate and b is the half chord. The convection velocity of the surface pressure is denoted by U_c. K_2 is the spanwise wavenumber of the surface pressure and $K_c = \frac{\omega}{U_c}$ is the convective wavenumber. Function sinc $y = \frac{\sin y}{y}$ and $\Pi_0\left(\bar{K}_c, \bar{K}_2\right)$ represents the energy of the fluctuating wall pressure at wavenumber K_2 and frequency ω. The form of Π_0 is discussed later. $I\left(\bar{K}_c, \bar{K}_2\right)$ is the radiation integral which accounts for how the fluctuating wall pressure at wavenumber K_2 and frequency ω radiates to the far field as sound. The radiation integral derived by Roger and Moreau [8] and including the effect of leading edge backscatter is used in the present work.

4.2 Near-field Radiation

The radiation of sound to the far field is obtained by considering a distribution of dipoles on the surface of the plate, with each dipole's force obtained from the disturbance pressure on the plate due to trailing edge scattering [6, 8]. As Amiet [6] and Roger and Moreau [8] were primarily concerned with far-field sound, the near-field component of the dipole's radiation kernel was not included. To investigate the impact of the near-field term of the dipole radiation kernel, consider the sound pressure radiated by a point force F oriented in the wall normal direction x_3, which corresponds to

$$p_a(\mathbf{x}, \omega) = F(\mathbf{y}, \omega) \frac{\partial G_h(\mathbf{x}, \mathbf{y}, \omega)}{\partial x_3} \tag{6}$$

$G_h(\mathbf{x}, \mathbf{y}, \omega)$ is the harmonic free-field Green's function between the source point **y** and receiver point **x**. In the context of the analytical scattering models of Amiet [6] and Roger and Moreau [8] the harmonic free-field Green's function is given by

$$G_h(\mathbf{x}, \mathbf{y}, \omega) = \frac{e^{ik_a R_t}}{4\pi S_0} \tag{7}$$

The derivative of equation (7) with respect to x_3 yields

$$
\begin{aligned}
\frac{\partial G_h(\mathbf{x}, \mathbf{y}, \omega)}{\partial x_3} &= \frac{e^{i k_a R_t}}{4 \pi S_0^2}(i k_a S_0 - 1) \frac{x_3}{S_0} \\
&= \frac{i k_a x_3 e^{i k_a R_t}}{4 \pi S_0^2} - \frac{x_3 e^{i k_a R_t}}{4 \pi S_0^3}
\end{aligned}
\tag{8}
$$

Here, $\frac{\partial R_t}{\partial x_3} \approx \frac{x_3}{S_0}$ has been used to simplify the derivation of equation (8) and retain the form of the radiation kernel used in Refs. [6, 8]. The first term on the right hand side of equation (8) represents the far-field component of the dipole radiated from a point force, with the second term representing the near-field component. To include the effects of the near-field component on trailing edge noise, equation (3) is modified as follows

$$
p_K(\mathbf{x}, \omega) = \left(\frac{i k_a x_3}{4 \pi S_0^2} - \frac{x_3}{4 \pi S_0^3}\right) \int_{-2b}^0 \int_{-L/2}^{L/2} \Delta P(K_1, K_2) e^{i k_a R_t} \, dy_1 \, dy_2
\tag{9}
$$

An expression for the autospectral density of the sound pressure including near-field effects becomes

$$
\begin{aligned}
S_{pp,\text{nf}}(\mathbf{x}, \omega) = {} & \left(\frac{i k_a x_3}{4 \pi S_0^2} - \frac{x_3}{4 \pi S_0^3}\right)^2 2 L^2 c \int_{-\infty}^{\infty} \Pi_0\left(\frac{\omega}{U_c}, K_2\right) \operatorname{sinc}^2\left(\frac{L}{2b}\left(\bar{K}_2 - \bar{k}\frac{x_2}{S_0}\right)\right) \\
& \times \left|I\left(\bar{K}_c, \bar{K}_2\right)\right|^2 d\bar{K}_2
\end{aligned}
\tag{10}
$$

It should be noted that equations (9) and (10) represent a significant simplification as variation in distance between source and receiver points has not been considered when calculating the derivative of the Green's function.

Fig. 5 compares the autospectral density of the acoustic pressure in the far-field and near-field respectively given by equations (5) and (10), for a receiver located directly above the trailing edge, with $\Pi_0(\bar{K}_c, \bar{K}_2) = 1$, $\forall \bar{K}_c, \bar{K}_2$. For spanwise wavenumbers $k_2/(\beta\mu) \leq 1$, where $\beta = \sqrt{1 - M^2}$ and $\mu = k_a b/\beta^2$, the intersection of the gust with the trailing edge travels faster than the speed of sound. These are called supercritical gusts and have the greatest contribution to the far-field sound produced by large span airfoils. For spanwise wavenumbers $k_2/(\beta\mu) \geq 1$, the intersection of the gust with the trailing edge travels slower than the speed of sound. These are called subcritical gusts and typically do not contribute significantly to the far-field sound. Fig. 5 shows that as the distance between source and field points decrease, the relative contribution of subcritical wavenumbers increases, with subcritical wavenumbers dominating the radiated pressure field for small separation distances. Fig. 5 also shows a significant increase in the radiated pressure when the near-field contribution from the dipole radiation kernel is included in the transfer function for small separation distances.
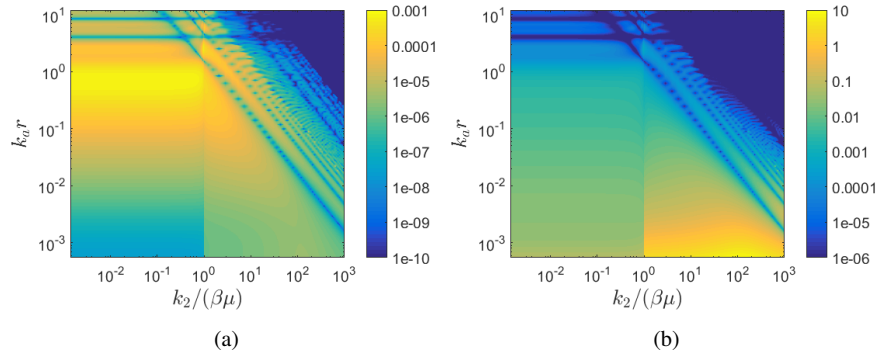
Fig. 5: Autospectral density of the radiated pressure for a unit gust input for (a) the far-field scattering model given by equation (5), and (b) the near-field scattering model given by equation (10). The vertical axis represents the distance between source and receiver points, normalised by the acoustic wavenumber k_a. The horizontal axis represents the spanwise wavenumber normalised by Graham's parameter which marks the cut-off between supercritical and subcritical wavenumbers

4.3 Reflections from Tunnel Walls

The tunnel walls are assumed to be perfectly rigid and the method of images is used to approximate the reflection of radiated pressure by the tunnel walls. Fig. 6 shows a schematic diagram of the method of images technique used to account for tunnel reflections. Virtual receivers are placed where mirror images of the actual receiver would be positioned beyond the tunnel walls. Pressures recorded at the actual receiver and each virtual receiver are combined together to predict the total response. In the present work, a total of 10 virtual receivers positioned beyond each wall of the tunnel was sufficient to obtain a converged solution.

Fig. 6 also shows that the spanwise extent of the plate was discretised into a finite number of spanwise strips. This is because the in-wall hydrophone is in close proximity to the plate and the distance from the plate to the hydrophone varies considerably based on spanwise position along the plate. By discretising the plate into a number of spanwise strips and calculating the hydroacoustic response of each strip individually, the influence of this spanwise variation in distance is captured in the results.

The coordinate system origin identified in Fig. 4 must be placed in the centre of each spanwise segment at the trailing edge. Hence, the source and receiver points vary considerably for each spanwise segment. Recognising that the phase information must be preserved when combining actual and virtual receiver pressures, and further, the autospectral density of the pressure predicted for each spanwise segment can simply be added together, the total autospectral density of the near-field pressure is given by:

- ● Actual receiver
- ○ Image receiver
- ▭ Blunt plate
- ▮ Plate spanwise segment
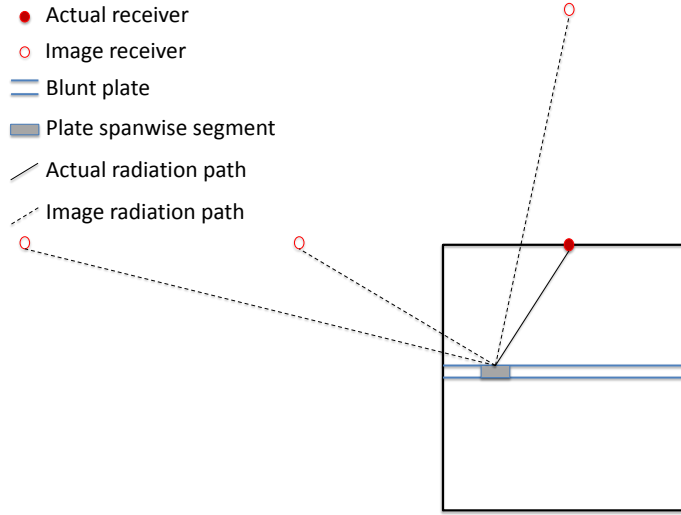- ╱ Actual radiation path
- ⋰ Image radiation path

Fig. 6: Schematic diagram illustrating the method of images used to approximate the effect of tunnel reflections on the radiated pressure. Orientation is from downstream of the plate, looking upstream with the in-wall hydrophone positioned above the plate. Flow is out of the page.

$$
S_{pp,\text{nf}}\left(\mathbf{x}, \omega\right) = \sum_{d=1}^{D} 2L_d^2 c \int_{-\infty}^{\infty} \Pi_0\left(\frac{\omega}{U_c}, K_2\right) \left(\sum_{n=1}^{N} \left[\left(\frac{i\, k_a x_{3,dn}}{4\pi S_{0,dn}^2} - \frac{x_{3,dn}}{4\pi S_{0,dn}^3} \right) \right. \right.
$$
$$
\left. \left. \text{sinc}\left(\frac{L_d}{2b}\left(\bar{K}_2 - \bar{k}_a \frac{x_{2,dn}}{S_{0,dn}}\right) \right) \times \left| I\left(\bar{K}_c, \bar{K}_2\right)\right| \right] \right)^2 \, \mathrm{d}\bar{K}_2 \qquad (11)
$$

where L_d is the span of spanwise segment d and D is the total number of segments. n is the receiver number, where $n = 1$ corresponding to the actual in-wall hydrophone location and N is the total number of receivers. $x_{2,dn}$ and $x_{3,dn}$ correspond to the 2nd and 3rd components of the position vector for the nth receiver location relative to the dth spanwise segment, with $S_{0,dn}$ the associated distance.

4.4 Estimating Pressure Field from LES

The final step in the analytical treatment of near-field pressure radiation from trailing edge scattering is to approximate the energy of the fluctuating wall pressure, $\Pi_0\left(\frac{\omega}{U_c}, K_2\right)$. In the present work, the following relationship is used [8]

$$\Pi_0 \left(\frac{\omega}{U_c}, K_2 \right) = \frac{1}{\pi} \Phi_{pp} (\omega) \, l_y (K_2, \omega) \tag{12}$$

where $\Phi_{pp} (\omega)$ is the autospectral density of the pressure near the blunt edge, and $l_y (K_2, \omega)$ is the spanwise correlation length of the pressure fluctuations.

Two alternate spanwise correlation length models are herein investigated. The model derived by Corcos [25] is widely used to estimate the cross-correlation of surface pressures under a turbulent boundary layer. The Corcos model is known to over-predict the low wavenumber response of the cross-correlation function, however it is easy to implement which adds to its popularity. The other model considered here is the model of Smol'yakov [26] which aims to address the deficiencies in the Corcos model. Details of these two models for the cross spectrumcan be found in Refs. [25, 26].

Combining equations (11) and (12) gives the final form of the analytical expression for near-field scattering as

$$S_{pp,\text{nf}} (\mathbf{x}, \omega) = \sum_{d=1}^{D} 2L_d^2 c \Phi_{pp} (\omega) \int_{-\infty}^{\infty} l_y (K_2, \omega) \left(\sum_{n=1}^{N} \left[\left(\frac{\mathrm{i} \, k_a x_{3,dn}}{4\pi S_{0,dn}^2} - \frac{x_{3,dn}}{4\pi S_{0,dn}^3} \right) \right. \right.$$
$$\left. \left. \text{sinc} \left(\frac{L_d}{2b} \left(\bar{K}_2 - \bar{k}_a \frac{x_{2,dn}}{S_{0,dn}} \right) \right) \times \left| I \left(\bar{K}_c, \bar{K}_2 \right) \right| \right] \right)^2 \mathrm{d} \, \bar{K}_2 \tag{13}$$

5 Results and Discussion

5.1 Hydrodynamic Flow Field

Fig. 7 presents isosurfaces of the Q-criterion coloured by the magnitude of the vorticity vector and shows the flow structures in the flow past the plate. Slightly downstream of the elliptical leading edge, the flow undergoes laminar to turbulence transition with the turbulent boundary layer developing along the length of the plate. At the blunt trailing edge the flow separates, forming two shear layers which roll up into vortices that are shed into the wake forming a von Karman vortex street. Fig. 7 shows that the vortices contain flow features with a wide range of scales. Hence the pressure waves produced at the vortex shedding frequency and its harmonics are likely to contain significant broadening of the tonal peaks. Also, the smaller scale turbulent structures in the boundary layer that convect past the blunt trailing edge are expected to produce broadband noise at higher frequencies. The results shown in Fig. 7 were prepared using the finest grid corresponding to Mesh 4 in Table 1, with near wall grid resolutions of $x^+ \approx 50$, $y^+ \approx 12$ and $z^+ \approx 60$.
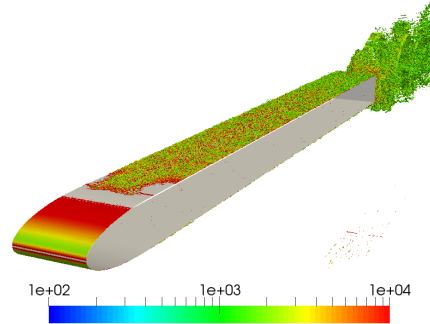
Fig. 7: Isosurfaces of Q-criteria showing flow structures, coloured by magnitude of vorticity

5.2 Surface Pressure Results and Measurements

Fig. 8 compares measured and predicted surface pressure at the 'near' pressure sensor location shown in Fig. 2. Fig. 8(a) shows the prediction obtained using the finest mesh resolution, corresponding to Mesh 4 in Table 1. The broadened tonal peaks correspond to the vortex shedding frequency and its harmonics. The LES simulation predicts that the vortex shedding frequency occurs at $St_h = 0.252$, which is within 7% of the measured value of 0.236. Within the frequency range from 10 Hz to 400 Hz, the autospectral density of the trailing edge pressure predicted with the LES follows the same general shape observed in the measured data, with the vortex shedding frequency and its second and third harmonics well captured. However, the magnitude of the autospectral density of the trailing edge pressure predicted by the LES within this frequency range is between 3 to 6 dB higher than the measured value. In this low frequency region, all of the LES meshes considered produced similar results. It is important to note that the same frequency bandwidth was used for both numerical and experimental data processing to ensure that the tonal peaks from both data sets encounter the same averaging. Overprediction at these low frequencies is attributed to the reduced span of the model with the periodic boundary conditions, which enforces greater coherence of the larger scale turbulence flow structures.

Fig. 8(b) shows the influence of mesh resolution on the higher frequency surface pressure predictions obtained using LES. Significant deviation is observed between the high frequency surface pressure predicted by the LES for Mesh 1, 2 and 3. The agreement between measured and predicted surface pressure improves substantially when Mesh 4 is used for the LES, with good agreement over most of the frequency range. However, even for Mesh 4 the predicted surface pressure begins to deviate as the frequency increases, indicating that additional grid refinement may be necessary to more accurately resolve the high frequency turbulence.

Fig. 9 presents the wavenumber-frequency decomposition of the surface pressures on the top surface of the plate. Fig. 9(a) shows the streamwise wavenumber distri-
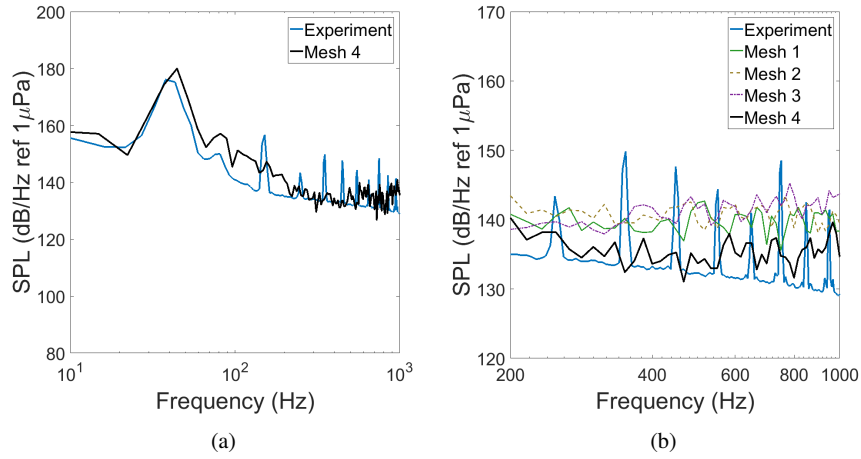
Fig. 8: (a) Autospectral density of the surface pressure at the trailing edge of the plate predicted using Mesh 4. (b) Influence of mesh resolution on the spectral content of the autospectral density of the trailing edge pressure

bution of the surface pressures as a function of angular frequency, ω. The majority of the surface pressure transport occurs between the two dashed black lines, representing convection velocities of 2.1 m/s and 7.5 m/s. This wide spread of convection velocities is due to the vortex shedding phenomenon, whereby the boundary layer is alternatively accelerated and decelerated by the roll-up and shedding of the trailing edge vortices. Fig. 9(b) presents the spanwise wavenumber distribution of the surface pressure as a function of angular frequency. The dominant concentration of spanwise wavenumbers to the surface pressure occurs at the vortex shedding frequency with the peak comprised of relatively low wavenumbers. This indicates that the large spanwise structures in the vortices makes the most significant contribution to the surface pressures on the plate. The dashed line in Fig. 9(b) represents a wavenumber 100 times larger than the cut-on wavenumber between subcritical and supercritical gusts. In Fig. 5, this corresponds to a vertical line at $k_2/(\beta\mu) = 100$ with energy to the left of this line having the greatest contribution to the radiated pressure. Hence, a large proportion of the energy represented in Fig. 9(b), corresponding to the energy to the right of the dashed line does not make a significant contribution to the radiated pressure.

5.3 Wall Mounted Hydrophone Results and Measurements

The autospectral density of the surface pressure near the blunt edge of the plate predicted using LES is combined with spanwise correlation length estimates of

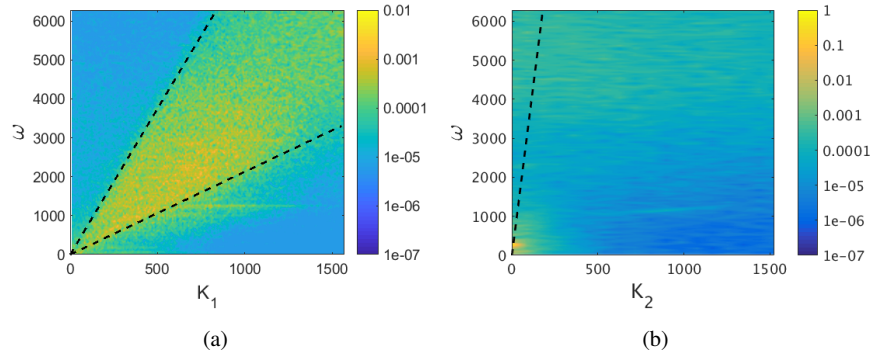(a)   (b)

Fig. 9: Wavenumber-frequency content of the surface pressures for (a) the streamwise wavenumbers, and (b) the spanwise wavenumbers, showing the energy contained at each wavenumber of the surface pressure for a given frequency

Corcos, $L_{y,C}$ and Smol'yakov $L_{y,S}$ and the near-field analytical scattering model given by equation (13). Including ten image receivers to account for reflections off the tunnel walls and discretising the span into eight spanwise segments, the pressure at the in-wall hydrophone location is estimated. Fig. 10(a) shows that there is excellent agreement between the sound pressure level (SPL) predicted from the LES/analytical scattering approach and the measured pressure at the wall mounted hydrophone when Smol'yakov's correlation length is used. The broadened tonal peak at the vortex shedding frequency is well predicted as is the broadband pressure at higher frequencies. The low frequency pressures were over-predicted when the spanwise correlation length of Corcos was applied. Fig. 10(a) also shows the background noise level measured for 8 m/s flow in the tunnel with no plate present. There is sufficient difference between background noise levels and the pressure levels measured at the wall mounted hydrophone when the plate is present to allow for meaningful comparison between numerical and measured data.

It is interesting to note that, although the surface pressure autospectral density at the trailing edge is over-predicted by the LES at low frequencies (see Fig. 8(a)), the estimated radiated pressure received at the in-wall hydrophone is in excellent agreement with the experimental measurements. The over-prediction in the surface pressure autospectral density at the trailing edge is caused by the reduced span of the model and the periodic boundary conditions enforcing greater coherence of the larger scale flow structures. Fig. 9(b) shows that only a small component of the total energy of the surface pressure fluctuations make a significant contribution to the radiated pressure. Hence, it seems likely that the boundary-condition-induced increase in surface pressure autospectral density is predominantly generated by wavenumber components that do not radiate efficiently from the trailing edge. This will be further investigated in future work.

Fig. 10(b) presents changes in predicted pressure from incremental modifications to the scattering model. The 'standard' curve represents the result obtained using

the analytical scattering model of Roger and Moreau [8], including leading edge back-scattering but considering only supercritical wavenumbers. The 'near-field' curve shows the incremental change when the influence of near-field effects are included in the analytical model. The 'subcritical' curve presents the additional effect arising from inclusion of subcritical wavenumbers. The 'reflections' curve further considers the reflection of the pressure from the rigid duct walls. All results presented in Fig. 10(b) have been calculated using the Smol'yakov length scale model. Fig. 10(b) show that both near-field effects and subcritical wavenumbers contribute significantly to the predicted pressure for this case study. Subcritical wavenumbers produce evanescent pressure waves which decay rapidly away from the source region and typically do not radiate to the far field as sound. However, in the current study, the receiver hydrophone is well within the near-field of the source region. Hence subcritical wavenumbers, near-field propagation effects and duct wall reflections must be included to give an accurate estimate of the pressure.
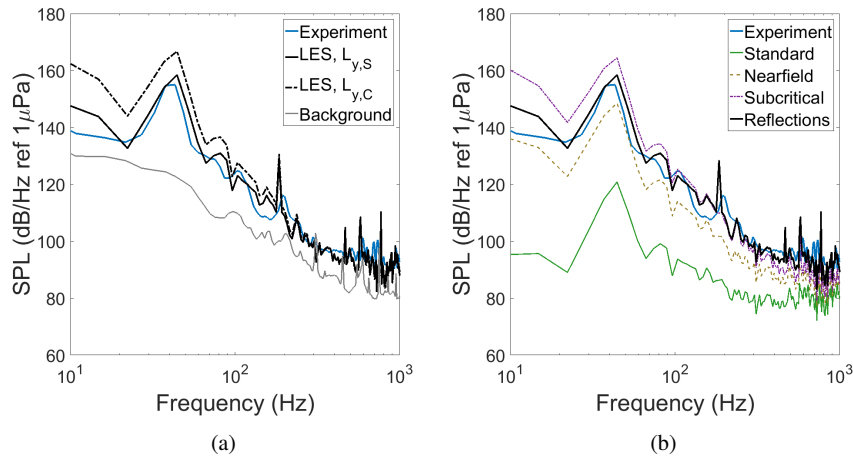

(a) (b)

Fig. 10: (a) Comparison of SPL predicted using the spanwise correlation length proposed by Smol'yakov, $L_{y,S}$ and Corcos, $L_{y,C}$. (b) Changes in predicted pressure with incremental enhancement of the analytical scattering model, using the correlation length of Smol'yakov

6 Conclusions

Experimental measurements and numerical predictions of the flow and noise produced by a blunt edged flat plate in a reverberant water tunnel has been presented. The experimental data indicates that the flow-induced noise levels measured at a

wall mounted hydrophone are significantly above the background noise levels of the tunnel and hence are suitable for validation of numerical predictions of the flow and noise. An analytical scattering model originally developed to predict far-field sound radiated from turbulent flow over the trailing edge of an airfoil in free stream conditions has been extended here to account for near-field effects and reflections from the side walls of the water tunnel. The LES of the flat plate, and subsequent prediction of the pressure fluctuations at the wall mounted hydrophone location using the near-field analytical scattering model agree well with the measured data. The results indicate that subcritical wavenumbers and near-field propagation effects must be included to give an accurate estimate of the pressure for the case considered here.

References

1. J. Seo and Y. Moon, "Aerodynamic noise prediction for long-span bodies," *Journal of Sound and Vibration*, vol. 306, pp. 564–579, 2007.
2. M. Wang, S. Moreau, G. Iaccarino, and M. Roger, "LES prediction of wall-pressure fluctuations and noise of a low-speed airfoil," *International Journal of Aeroacoustics*, vol. 8, pp. 177–198, 2009.
3. W. R. Wolf and S. K. Lele, "Acoustic analogy formulations accelerated by fast multipole method for two-dimensional aeroacoustic problems," *AIAA Journal*, vol. 48, pp. 2274–2285, 2010.
4. M. Karimi, P. Croaker, N. Peake, and N. Kessissoglou, "Acoustic scattering for rotational and translational symmetric structures in nonuniform potential flow," *AIAA Journal*, vol. 55, no. 10, pp. 3318–3327, 2017.
5. R. K. Amiet, "Acoustic radiation from an airfoil in a turbulent stream," *Journal of Sound and Vibration*, vol. 41, pp. 407–420, 1975.
6. R. K. Amiet, "Noise due to turbulent flow past a trailing edge," *Journal of Sound and Vibration*, vol. 47, pp. 387–393, 1976.
7. M. S. Howe, "Edge-source acoustic Green's function for an airfoil of arbitrary chord, with application to trailing-edge noise," *Quarterly Journal of Mechanics and Applied Mathematics*, vol. 54, pp. 139–155, 2001.
8. M. Roger and S. Moreau, "Back-scattering correction and further extension of Amiet's trailing-edge noise solution. Part 1: Theory," *Journal of Sound and Vibration*, vol. 286, pp. 477–506, 2005.
9. M. C. Jacob, D. Boudet, D. Casalino, and M. Michard, "A rod-airfoil experiment as a benchmark for broadband noise modelling," *Theoretical and Computational Fluid Dynamics*, vol. 19, pp. 171–196, 2005.
10. W. J. Devenport, J. K. Staubs, and S. A. L. Glegg, "Sound radiation from real airfoils in turbulence," *Journal of Sound and Vibration*, vol. 329, pp. 3470–3483, 2010.
11. D. Moreau, L. Brooks, and C. Doolan, "The effect of boundary layer type on trailing edge noise from sharp-edged flat plates at low-to-moderate Reynolds number," *Journal of Sound and Vibration*, vol. 331, pp. 3976–3988, 2012.
12. D. J. Moreau, C. J. Doolan, W. N. Alexander, T. W. Meyers, and W. J. Devenport, "Wall-mounted finite airfoil-noise production and prediction," *AIAA Journal*, vol. 54, no. 5, pp. 1637–1651, 2016.
13. S. Ianniello, R. Muscari, and A. Di Mascio, "Ship underwater noise assessment by the Acoustic Analogy part I: nonlinear analysis of a marine propeller in a uniform flow," *Journal of Marine Science and Technology*, vol. 19, no. 4, pp. 547–570, 2013.

14. S. Ianniello, R. Muscari, and A. Di Mascio, "Ship underwater noise assessment by the Acoustic Analogy part II: hydroacoustic analysis of a ship scaled model," *Journal of Marine Science and Technology*, vol. 19, no. 1, pp. 52–74, 2014.

15. S. Ianniello, R. Muscari, and A. Di Mascio, "Ship underwater noise assessment by the Acoustic Analogy part III: measurements versus numerical predictions on a full-scale ship," *Journal of Marine Science and Technology*, vol. 19, no. 2, pp. 125–142, 2014.

16. S. Ianniello, "The Ffowcs Williams-Hawkings equation for hydroacoustic analysis of rotating blades. Part 1. The rotpole," *Journal of Fluid Mechanics*, vol. 797, pp. 345–388, 2016.

17. M. Cianferra, V. Armenio, and S. Ianniello, "Hydroacoustic noise from different geometries," *International Journal of Heat and Fluid Flow*, vol. 70, pp. 348–362, 2018.

18. S. Glegg and W. Devenport, "Chapter 5 - the Ffowcs Williams and Hawkings equation," in *Aeroacoustics of Low Mach Number Flows* (S. Glegg and W. Devenport, eds.), pp. 95 – 114, Academic Press, 2017.

19. M. Roger and S. Moreau, "Addendum to the back-scattering correction of Amiet's trailing-edge noise model," *Journal of Sound and Vibration*, vol. 331, pp. 5383–5385, 2012.

20. P. A. Brandner, Y. Lecoffre, and G. J. Walker, "Design considerations in the development of a modern cavitation tunnel," in *Proceedings of the 16th Australasian Fluid Mechanics Conference*, (Crown Plaza, Gold Coast, Australia), 3-7 December 2007.

21. C. Doolan, P. Brandner, D. Butler, B. Pearce, D. Moreau, and L. Brooks, "Hydroacoustic characterisation of the AMC cavitation tunnel," in *Acoustics 2013 - Victor Harbor*, (Victor Harbor, Australia), 2013.

22. F. Nicoud and F. Ducros, "Subgrid-scale stress modelling based on the square of the velocity gradient tensor," *Flow, Turbulence and Combustion*, vol. 62, no. 3, pp. 183–200, 1999.

23. D. B. Spalding, "A single formula for the "law of the wall"," *Journal of Applied Mechanics*, vol. 28, pp. 455–458, 1961.

24. H. G. Weller, G. Tabor, H. Jasak, and C. Fureby, "A tensorial approach to computational continuum mechanics using object-oriented techniques," *Computer in Physics*, vol. 12, pp. 620–631, 1998.

25. G. M. Corcos, "The structure of the turbulent pressure field in boundary-layer flows," *Journal of Fluid Mechanics*, vol. 18, pp. 353–378, 1964.

26. A. V. Smol'yakov, "A new model for the cross spectrum and wavenumber–frequency spectrum of turbulent pressure fluctuations in a boundary layer," *Acoustical Physics*, vol. 52, pp. 331–337, 2006.